PAPER

Check for updates

Broadly tunable full-visible-spectrum ZnS/ZnO:Mn²⁺ composite microphosphor for warm WLED applications

Hoang Gia Chuc,[a] Pham Minh Tri,[a] Manh Trung Tran, [ID] *[a] Do Quang Trung, [ID] *[b] Nguyen Tu, [ID] [b] Nguyen Van Du,[b] Nguyen Minh Hieu, [ID] [a] Nguyen Duc Trung Kien,[c] Ta Ngoc Bach,[d] Le Tien Ha, [ID] [e] Nguyen Duy Hung,[f] Dao Xuan Viet,[f] Ngo Ngoc Ha[a] and Pham Thanh Huy [ID] [a]

Phosphor development for warm white LEDs (w-WLEDs) is key to enhancing light quality, energy efficiency, stability, and environmental sustainability. Mn²⁺-doped phosphors, known for their broad visible emission, are especially promising for UV-pumped w-WLEDs. While halide and garnet systems show potential, they suffer from toxicity and complex synthesis, making ZnO and ZnS attractive, stable alternatives. In this study, tunable full-visible-spectrum ZnS/ZnO:Mn²⁺ phosphors were synthesized *via* a simple thermal diffusion method. Structural analyses (XRD, Raman) revealed temperature-driven phase evolution, while PL and PLE measurements confirmed strong UV absorption and broad 400–700 nm emission from both host and Mn²⁺ centers. Emission was effectively tuned by Mn²⁺ concentration, with the ZnS/ZnO:0.1% Mn²⁺ sample emitting warm white light (CIE: $x = 0.35$, $y = 0.37$; CCT: 4920 K; decay time: 0.35 ms; activation energy: 0.31 eV). A phosphor-coated LED prototype demonstrated high luminous efficacy (127.7 lm per W), CIE coordinates $(x, y) = (0.4974, 0.3405)$, CRI of 72, and a correlated color temperature (CCT) of 2506 K, suitable for warm lighting applications.

1 Introduction

Light is a crucial factor affecting the survival of living organisms. Finding an artificial light source that closely mimics sunlight remains a significant challenge, yet it represents an area of immense research potential. With this goal in mind, humans have developed successive generations of lighting technologies such as fluorescent lamps, compact fluorescent lamps, and now, LEDs and WLEDs. These technologies are widely adopted due to advantages such as low power consumption, high luminous efficiency, and the absence of mercury, allowing them to dominate the lighting market compared to other options.[1,2] The current method of producing WLEDs involves combining blue LED chips with the commercial yellow phosphor YAG:Ce³⁺ ($Y_3Al_5O_{12}$:Ce³⁺),[3,4] which offers good conversion efficiency. However, the blue light emitted from the blue chip can suppress melatonin—a hormone responsible for regulating circadian rhythms—potentially leading to sleep disturbances. Additionally, the emission spectrum of commercial WLEDs lacks green and red regions, which reduces color rendering accuracy.

Thanks to their broad-band emission, which surpasses that of many traditional rare-earth ions (Eu²⁺, Ce³⁺, *etc.*) and other transition metal ions (Bi²⁺, Bi³⁺, Ni²⁺, *etc.*), Mn²⁺-doped phosphors hold strong potential for UV-driven tunable warm WLED applications.[5] Notable examples include ($C_6H_{18}N_2O_2$) PbBr₄:Mn²⁺,[6] BaAl₁₂O₁₉:Mn²⁺, SrAl₁₂O₁₉:Mn⁴⁺,[7] Na₃LuSi₂O₇:-Eu²⁺,Mn²⁺.[8] However, these materials often face challenges such as moisture sensitivity, lead toxicity, limited thermal stability, complex synthesis, doping imbalance, and performance inconsistency due to sensitivity to doping and thermal quenching under high-power operation. Several studies have shown that wide bandgap semiconductors like ZnO and ZnS are promising alternatives to complex oxides as host matrices,[9–11] offering strong UV resistance and excellent compatibility with transition metal ions.[12–14] Recently, ZnS/ZnO-based materials, including ZnS/ZnO phosphors[15] and ZnS/ZnO:Mn²⁺ nanobelts,[13] have been successfully fabricated,

[a]Faculty of Materials Science and Engineering, Phenikaa School of Engineering, Phenikaa University, Yen Nghia Ha-Dong District, Hanoi, 12100, Vietnam. E-mail: trung.tranmanh@phenikaa-uni.edu.vn

[b]Faculty of Fundamental Science, Phenikaa University, Yen Nghia Ha-Dong District, Hanoi, 12100, Vietnam. E-mail: trung.doquang@phenikaa-uni.edu.vn

[c]Faculty of Electrical and Electronic Engineering, Phenikaa University, Yen Nghia, Ha-Dong District, Hanoi 10000, Vietnam

[d]Institute of Materials Science, Vietnam Academy of Science and Technology, 18 Hoang Quoc Viet Street, Cau Giay District, Hanoi 10000, Vietnam

[e]Institute of Science and Technology, TNU-University of Sciences, Thai Nguyen, 250000, Vietnam

[f]Department of Electronic Materials and Devices, School of Materials Science and Engineering, Hanoi University of Science and Technology (HUST), 01 Dai Co Viet Street, Hanoi 10000, Vietnam
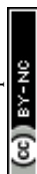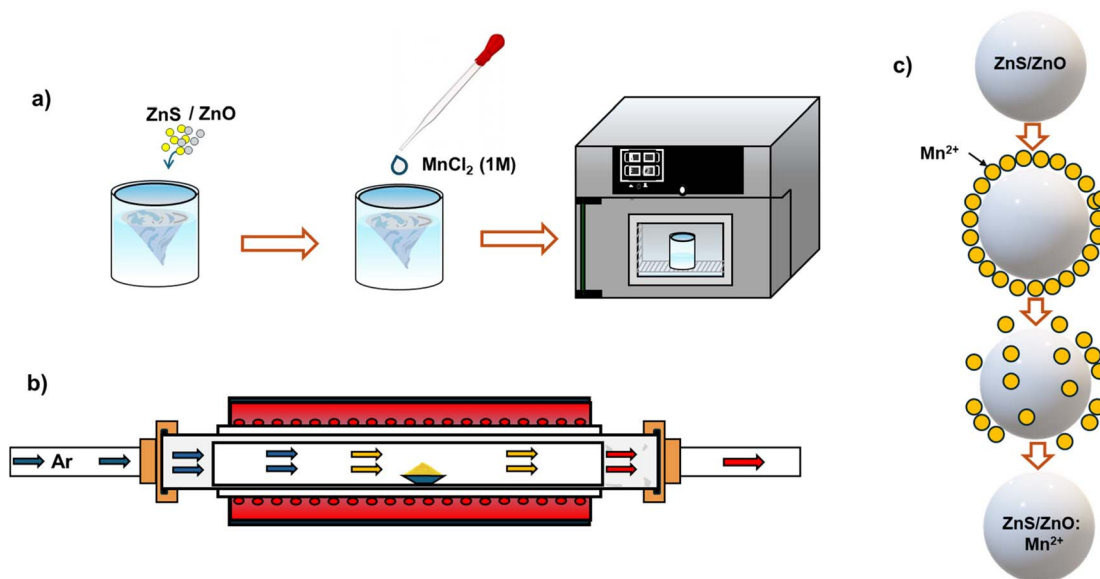
Fig. 1 (a and b) Schematic of the ZnS/ZnO:Mn^{2+} fabrication process; (c) illustration of the Mn^{2+} diffusion mechanism.

exhibiting full-visible-spectrum emission. However, their practical application remains limited by complex fabrication processes and poor scalability. To overcome these issues, surface diffusion has emerged as an efficient doping technique, enabling scalable synthesis of phosphors for warm white LED applications.[16]
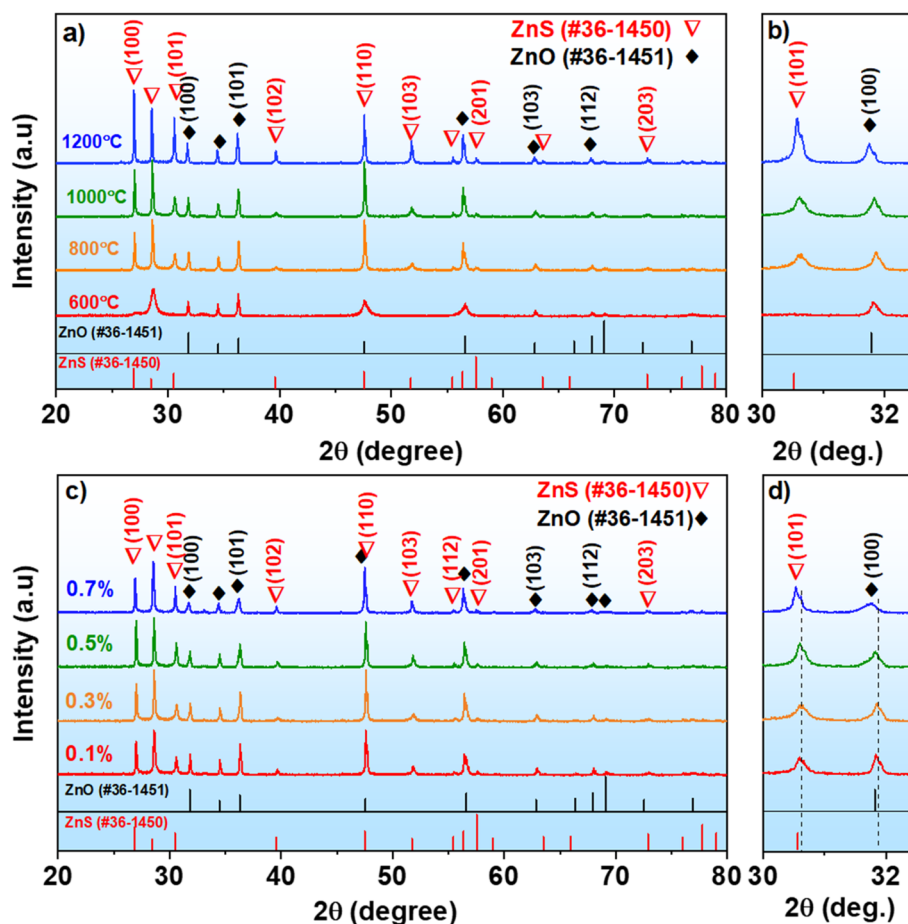

Fig. 2 (a and b) X-ray diffraction (XRD) patterns of the ZnS/ZnO:0.1% Mn^{2+} sample sintered at 600–1200 °C. (c and d) XRD patterns of ZnS/ZnO:x% Mn^{2+} samples (x = 0.1–0.7) sintered at 1000 °C in an argon gas atmosphere.
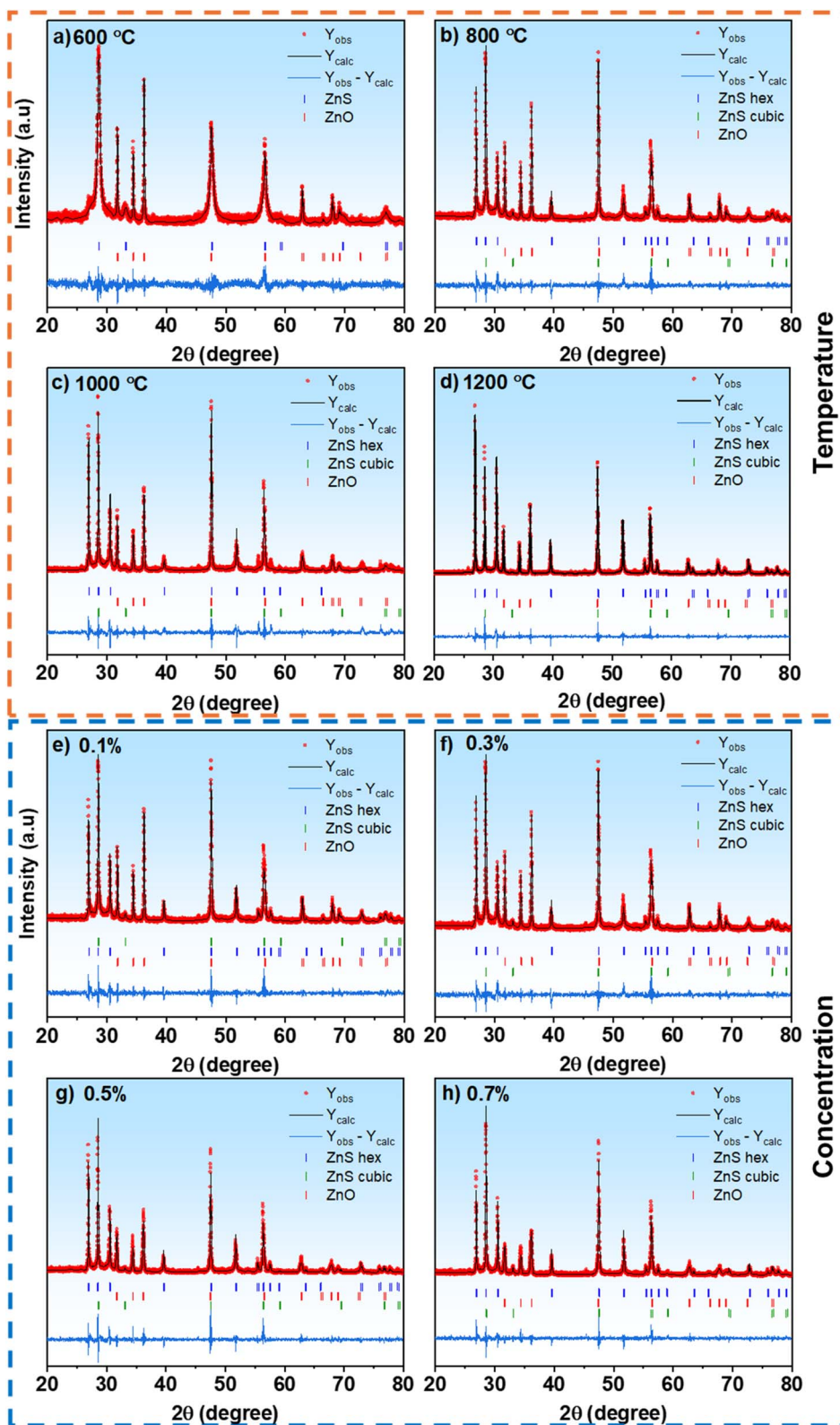
Fig. 3 Rietveld refinement analysis of (a–d) ZnS/ZnO:0.1% Mn^{2+} samples sintered at 600–1200 °C and (e–h) of ZnS/ZnO:x%Mn^{2+} samples (x = 0.1–0.7) sintered at 1000 °C.

Herein, we developed a ZnS/ZnO:Mn^{2+} material using a surface diffusion method. ZnS/ZnO samples doped with 0.1% Mn^{2+} were annealed in an argon atmosphere for 2 hours at various temperatures. These samples have dual emission bands, including 450–550 nm from the ZnS/ZnO host and a strong 560–700 nm band from Mn^{2+} ions. The influence of annealing temperature on crystal phase formation was also systematically investigated.

2 Experimental

2.1 Synthesis process of Mn²⁺ doped ZnS/ZnO materials

High-purity starting materials, including ZnS (99.9%, Merck), ZnO (99.9%, Merck), and $MnCl_2 \cdot 4H_2O$ (99.9%, Merck), were used to synthesize the ZnS/ZnO:Mn²⁺ phosphors *via* a facile thermal diffusion method.[16,17] ZnS and ZnO were first ball-milled at 500 rpm for 30 minutes, then stirred in 200 mL of deionized water at room temperature for 1 hour to form a uniform ZnS/ZnO mixture. A 1 mol per L $MnCl_2 \cdot 4H_2O$ solution was gradually added, allowing Mn²⁺ ions to diffuse into the host lattice. The resulting white mixture was dried at 120 °C for 10 hours (Fig. 1a), then sintered in argon gas at temperatures ranging from 600 to 1200 °C for 2 hours to obtain the final Mn²⁺-doped ZnS/ZnO powder (Fig. 1b). The thermal diffusion mechanism is illustrated in Fig. 1c.[16]

2.2 Characterization

The phase compositions and crystalline structures of all samples were determined using an X-ray powder diffractometer (XRD D8 advanced) with CuKα radiation ($\lambda = 0.1541$ Å). Surface morphology and chemical composition were examined through FESEM images and EDS spectra based on JSM-7600F equipment. Raman spectra were recorded using an XploRA Plus Raman microscope (Horiba, France) with a 532 nm laser excitation source. The binding energies of Zn, S, O, and Mn were analyzed with an Al Kα X-ray photoelectron spectrometer (XPS, Thermo Scientific, USA). The optical properties of the samples were measured using a photoluminescence spectrophotometer (Nanolog Horiba) with excitation from a 450 W xenon discharge lamp. The optical properties of the LED device were assessed using a Gamma Scientific GS-1290 spectroradiometer (RadOMA).

3 Results and discussion

Fig. 2a and b show the XRD patterns of ZnS/ZnO:0.1% Mn²⁺ powers sintered in argon gas at temperatures ranging from 600

to 1200 °C for 6 hours. At 600 °C, the cubic ZnS phase predominates, displaying characteristic peaks at $2\theta = 28.54°$, 33.32°, 47.53°, and 56.31°, corresponding to the (111), (200), (220), and (311) planes, respectively.[18-20] As the temperature increases to between 800 and 1200 °C, the hexagonal ZnS phase begins to appear, with new peaks at $2\theta = 26.92°$, 28.65°, 30.50°, and 39.50°, which are associated with the (100), (002), (101), and (102) diffraction planes of hexagonal ZnS (#36-1450).[13,21,22] Concurrently, the hexagonal ZnO phase becomes more apparent, indicated by peaks at $2\theta = 31.80°$, 34.40°, and 36.23°, corresponding to the (100), (002), and (101) diffraction planes.[13,21,23-25] The intensities of these peaks gradually increase with higher sintering temperatures, suggesting an improvement in the crystalline quality of both ZnS and ZnO.

Fig. 2c and d illustrate the XRD patterns of ZnS/ZnO:x% Mn²⁺ ($x = 0.1-0.7$) powders sintered at 1000 °C for 6 hours in

Table 2 The fitted values from Rietveld refinement of the XRD data for the ZnS/ZnO:x% Mn²⁺ ($x = 0.1-0.7$) samples sintered at 1000 °C

Concentration (%)	Phase	Lattice parameters (Å)		Lattice volume, V (Å³)
		a	c	
0.1	ZnS (hex)	3.82269	6.25952	79.215
	ZnS (cubic)	5.40726		158.100
	ZnO	3.25041	5.20473	47.622
	$R_p = 13.6\%$	$R_{exp} = 14.70\%$		$\chi^2 = 1.52$
0.3	ZnS (hex)	3.82452	6.26202	79.323
	ZnS (cubic)	5.41123		158.448
	ZnO	3.25404	5.20901	47.767
	$R_p = 15.8\%$	$R_{exp} = 16.18\%$		$\chi^2 = 1.59$
0.5	ZnS (hex)	3.82404	6.26282	79.313
	ZnS (cubic)	5.41008		158.348
	ZnO	3.25807	5.21341	47.926
	$R_p = 15.1\%$	$R_{exp} = 15.12\%$		$\chi^2 = 1.67$
0.7	ZnS (hex)	3.82628	6.26476	79.431
	ZnS (cubic)	5.41283		158.589
	ZnO	3.26127	5.21733	48.056
	$R_p = 14.0\%$	$R_{exp} = 15.87\%$		$\chi^2 = 1.37$

Table 1 The fitted values from Rietveld refinement of ZnS/ZnO:0.1% Mn²⁺ samples sintered at 600–1200 °C

Temperature (°C)	Phase	Lattice parameters (Å)		Lattice volume, V (Å³)	Phase fraction (%)
		a	c		
600	ZnS (cubic)	5.39832		157.157	∼67.33
	ZnO	3.25022	5.20539	47.593	∼32.67
	$R_p = 14.3\%$	$R_{exp} = 15.81\%$		$\chi^2 = 1.48$	
800	ZnS (hex)	3.82515	6.26245	79.355	23.79
	ZnS (cubic)	5.41190		158.508	41.07
	ZnO	3.25259	5.20815	47.717	35.14
	$R_p = 13.6\%$	$R_{exp} = 14.86\%$		$\chi^2 = 1.58$	
1000	ZnS (hex)	3.82531	6.26532	79.397	27.67
	ZnS (cubic)	5.41238		158.549	36.95
	ZnO	3.25778	5.21191	47.904	35.68
	$R_p = 15.1\%$	$R_{exp} = 14.57\%$		$\chi^2 = 1.99$	
1200	ZnS (hex)	3.81957	6.25292	79.095	∼58.20
	ZnS (cubic)	5.40373		157.790	5.62
	ZnO	3.25556	5.20908	47.871	∼36.18
	$R_p = 12.6\%$	$R_{exp} = 14.81\%$		$\chi^2 = 1.31$	

argon. As shown in Fig. 2c, XRD patterns indicate that the structure of both ZnS and ZnO remains unchanged as the concentration of Mn^{2+} increases. However, the diffraction peak shifts towards a smaller 2θ angle with increasing Mn^{2+} concentration (Fig. 2d), indicating the substitution of larger-radius ions for smaller-radius ions in the ZnS/ZnO lattice.[26]

The crystallite size can be estimated using the Scherrer eqn (1):[27]

$$D = \frac{k\lambda}{\beta \times \cos(\theta)} \qquad (1)$$

where D is the crystal size, λ is the X-ray wavelength (in this study, Cu Kα radiation, $\lambda = 0.154$ nm); θ is the Bragg angle (in degrees), k is the shape factor (0.94), β is the full width at half maximum (FWHM) of the diffraction peak. The FWHM value of

the ZnS peak at approximately 28.6° decreases as the sintering temperature increases from 600 °C to 1200 °C, indicating larger and more refined ZnS crystals at higher temperatures. Using the Scherrer eqn (1), the average crystal sizes are estimated at approximately 29.34 nm for ZnS and 14.99 nm for ZnO. Additionally, Rietveld refinement analysis of ZnS/ZnO:0.1% Mn^{2+} samples sintered at 600–1200 °C was presented in Fig. 3a. The phase proportions, lattice parameters and unit cell volumes of the ZnS and ZnO phases were listed in Table 1.[28] The low value of χ^2 indicates a strong agreement between the experimental and the calculated data. At 600 °C, two distinct phases – cubic ZnS and hexagonal ZnO – were identified in a 7 : 3 ratio. As the temperature increases, the hexagonal ZnS phase emerges, and the crystallinity of both ZnS and ZnO phases becomes more refined.
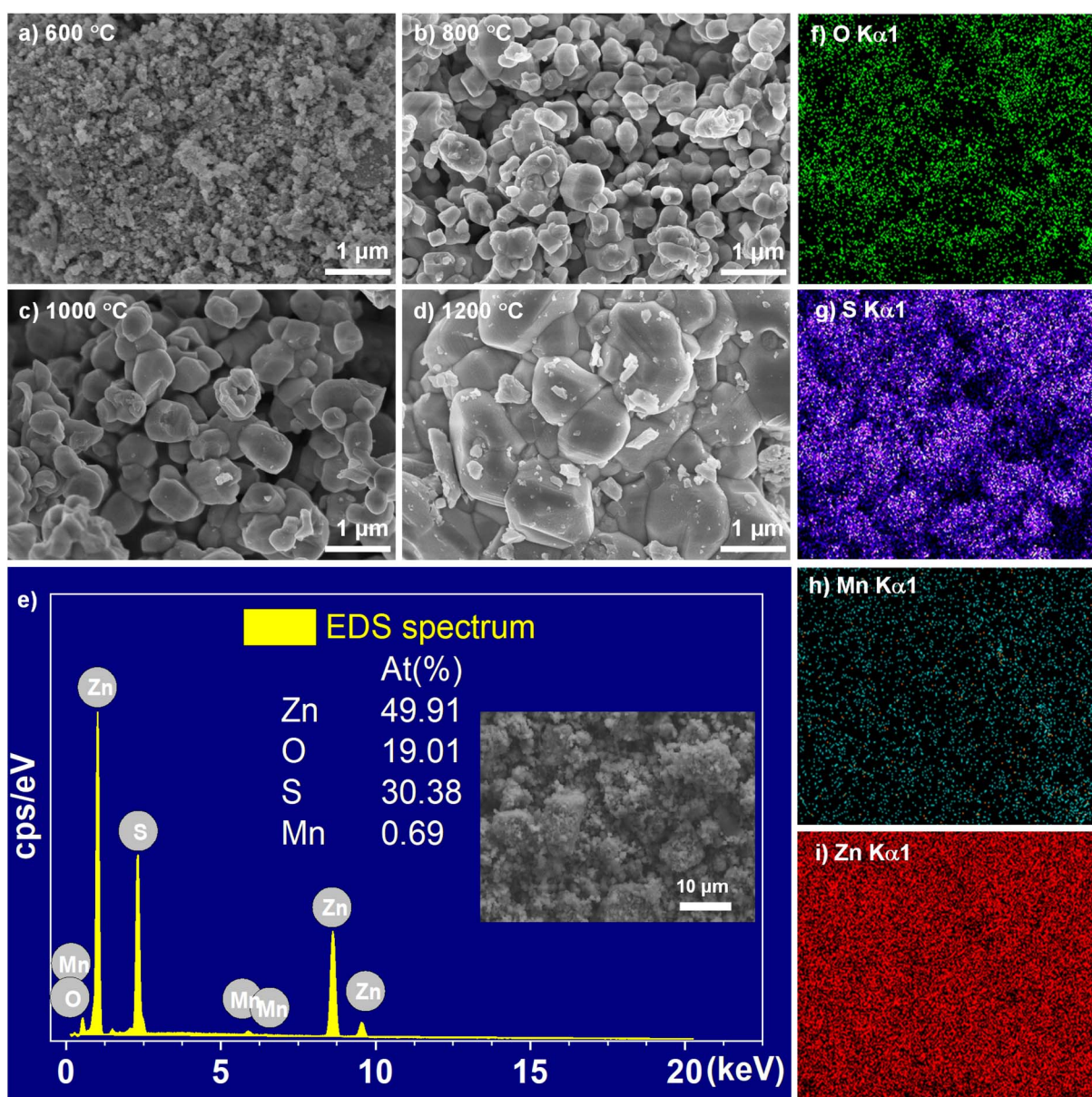

Fig. 4 (a–d) SEM images of ZnS/ZnO:0.1% Mn^{2+} samples sintered for 2 h in the argon at various temperatures of 600–1200 °C, (e) EDS elements and (f–i) EDS mapping spectra of ZnS/ZnO:0.1% Mn^{2+} sample sintered in argon at 1000 °C for 2 h.

Rietveld refinement analysis of ZnS/ZnO:x% Mn^{2+} samples (x = 0.1–0.7) sintered at 800 °C in an argon atmosphere were shown in Fig. 3b. All fitted values including lattice parameters, volume, phase composition and standard deviations were illustrated in Table 2. As shown in Table 2, the phosphors contain both ZnS and ZnO phases, confirming the formation of a composite structure. With increasing Mn doping from 0.1% to 0.7%, the lattice constants and unit cell volumes of both phases increase, suggesting the substitution of larger Mn^{2+} (r = 0.83 Å) ions for smaller Zn^{2+} (r = 0.74 Å) ions in the ZnS/ZnO lattice.[26]

Fig. 4a–d presents SEM images of ZnS/ZnO:0.1% Mn^{2+} phosphors sintered at temperatures from 600 °C to 1200 °C, showing clear microstructural evolution. At 600 °C, particles appear small, irregular, and highly agglomerated, indicating incomplete crystallization. By 800 °C, the particles become more defined with reduced agglomeration, indicating the onset of significant grain growth. At 1000 °C, the crystallites enlarge, surfaces smooth out, and overall uniformity improves, reflecting enhanced crystallinity. Finally, at 1200 °C, particles grow significantly larger and faceted, with clear grain boundaries due to sintering and densification. This temperature-driven evolution closely aligns with the crystallinity improvements observed in the XRD results.

Fig. 4e presents the EDS spectrum of the ZnS/ZnO:0.1% Mn sample sintered in argon at 1000 °C for 2 h, confirming the presence of Zn (49.91 at%), S (30.38 at%), O (19.01 at%), and Mn (0.69 at%) with no detectable impurities, indicating high purity. The corresponding EDS elemental maps (Fig. 4f–i) further demonstrate the uniform distribution of all constituent elements across the material.

Fig. 5 illustrates the Raman spectra of ZnS/ZnO:x% Mn^{2+} (x = 0.1–0.7) samples sintered at 1000 °C for 2 hours in argon gas, measured using a 785 nm laser across 100800 cm^{-1}.[26,29] As shown in Fig. 5a, ZnS exhibits characteristic peaks at 157, 217, 268, 348, and 412 cm^{-1},[30,31] while ZnO features are observed at 98, 375, 437 and 535 cm^{-1}.[29,32] In Fig. 5b, increasing Mn^{2+} content leads to reduced intensity and a blue shift in Raman peaks, likely due to the substitution of larger Mn^{2+} (r = 0.83 Å) ions for smaller-radius Zn^{2+} (r = 0.74 Å) ions in the ZnS/ZnO lattice.[33,34]

Fig. 6a shows the XPS survey spectrum of the ZnS/ZnO:0.1% Mn^{2+} sample sintered at 1000 °C for 2 hours in argon, calibrated using the binding energy of carbon (C 1s) with a reference peak at 284.6 eV.[15,35] Fig. 6b, the Zn 2p$_{3/2}$ peak is observed at approximately 1021.6 eV, consistent with the binding energy of Zn^{2+} in ZnS/ZnO.[15] Fig. 6c shows S 2p peaks at ~161.9 eV and ~163.2 eV, corresponding to the S 2p$_{3/2}$ và S 2p$_{1/2}$ states.[21] The O 1s spectrum reveals two component peaks: one at around 530.5 eV, attributed to O–Zn bonds in the host lattice,[13] and another at approximately 532.0 eV, likely associated with adsorbed H$_2$O or O$_2$ on the surface.[35] In Fig. 6d, the Mn 2p spectrum shows a peak at ~640.0 eV, confirming the presence of Mn^{2+} ions in the ZnS and ZnO matrix.[33,36]

Fig. 7a and b show the PLE spectra mentioned at 466 nm and 586 nm of ZnS/ZnO:0.1% Mn^{2+} samples sintered at 600–1200 °C for 2 hours in argon. A strong absorption band appears at 333–339 nm, attributed to ZnS band-to-band transitions,[21,24,37] and a weaker peak at 372 nm corresponds to ZnO transitions.[25,38] Fig. 7c and d show the PL spectra and responding to the normalized PL spectra of undoped ZnS/ZnO and ZnS/ZnO:0.1% Mn^{2+} samples sintered at different temperatures in the range of 600–1200 °C. The undoped ZnS/ZnO sample exhibits a strong blue-green emission peaking at 495 nm, linked to defect-related emissions.[39–42] In contrast, the ZnS/ZnO:0.1% Mn^{2+} samples show an additional broad emission centered at 586 nm, attributed to the $^4T_1 \rightarrow {}^6A_1$ transition of Mn^{2+} ions in the ZnS/
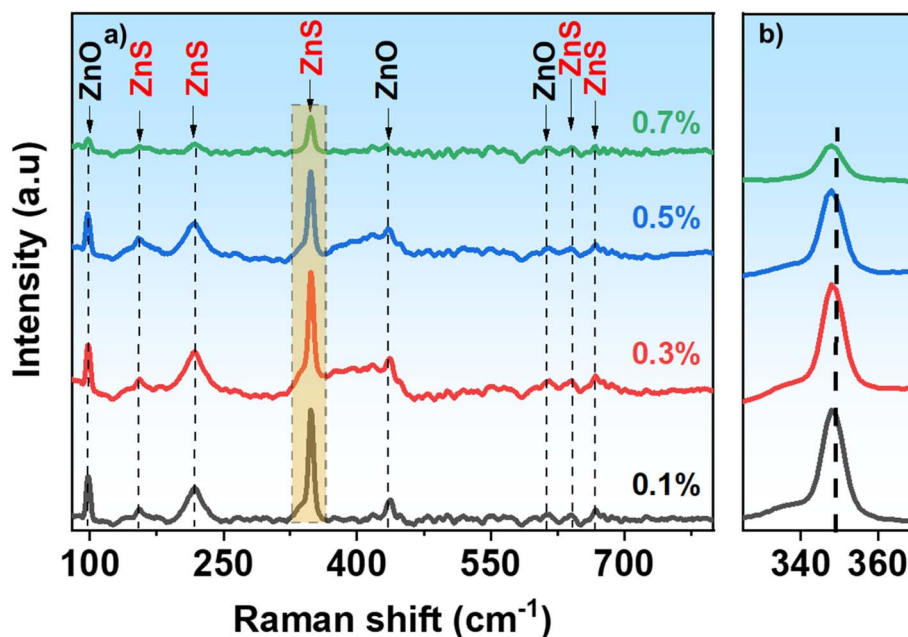

Fig. 5 (a) Raman spectra of ZnS/ZnO:x% Mn^{2+} (x = 0.1–0.7) samples sintered at 1000 °C for 2 h in argon; (b) enlarged view of the ZnS vibrational mode at 348 cm^{-1}.
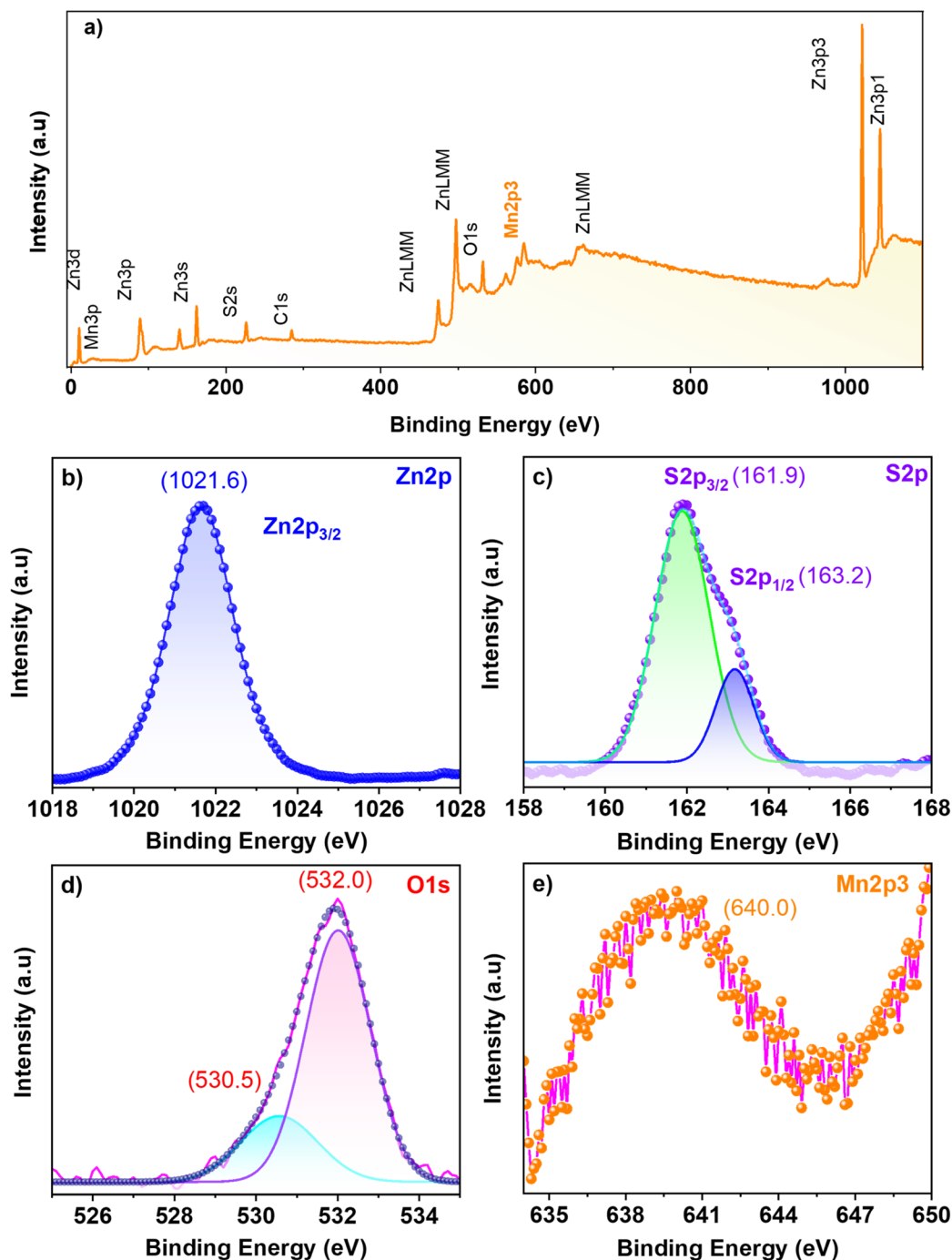
Fig. 6 XPS spectra of (a) survey spectrum, (b) Zn 2p, (c) S 2p, (d) O 1s and (e) Mn 2p of ZnS/ZnO:0.1% Mn^{2+} samples sintered at 1000 °C for 2 hours in argon.

ZnO lattice.[13,22,43] The emission intensity ratio between the yellow-orange and blue-green regions varies significantly with sintering temperature. Yellow-orange emission peaks at 800 °C, while blue-green emission is strongest at 1000 °C, likely due to competition between Mn^{2+} transitions and intrinsic defect emissions in ZnS/ZnO.[44]

To further elucidate this observation, the PL spectra of ZnS/ZnO:0.1% Mn^{2+} samples sintered at 600 to 1200 °C were

deconvoluted into three bands corresponding to the blue, green, and yellow regions, as illustrated in Fig. 8(a–d).

Table 3 presents the yellow-orange to blue-green emission intensity ratios for samples dried at various temperatures. The sample annealed at 1000 °C shows the most optimal ratio for full-spectrum WLED applications, making it the chosen condition for subsequent experiments.

Fig. 9a and b illustrates the PLE and PL spectra excited at 330 nm for ZnS/ZnO:x Mn^{2+} (x = 0.1–0.7%) sintered at 1000 °C.
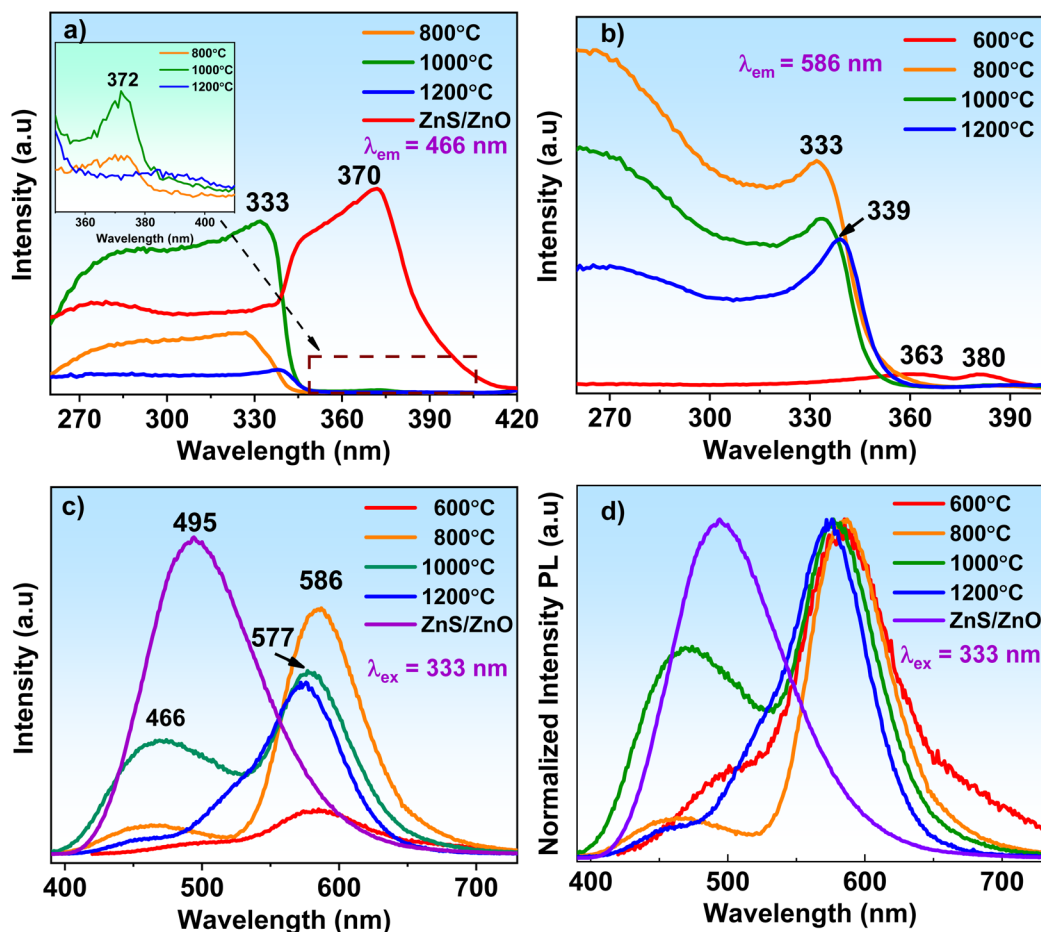
Fig. 7 PLE spectra mentioned at 466 nm (a) and 586 nm (b) of ZnS/ZnO:0.1% Mn^{2+} samples sintered at 1000 °C for 2 hours in argon. PL spectra excited at 333 nm (c) and corresponding to the normalized PL spectra (d) of ZnS/ZnO:0.1% Mn^{2+} samples sintered at 1000 °C for 2 hours in an argon gas environment.

All spectra feature a prominent yellow-orange emission band attributed to the $^4T_1 \rightarrow {}^6A_1$ transition of Mn^{2+} ions and a weaker blue-green emission related to intrinsic defects in the ZnS and ZnO hosts.

For the yellow-orange emission band, the PL intensity initially increased with Mn^{2+} concentration from 0.1% to 0.5%, reaching a maximum at 0.5% Mn concentration before declining at higher concentrations – a typical luminescence quenching behavior (Fig. 9b). Meanwhile, the blue-green emission steadily weakened with increased Mn^{2+} content, likely due to competition between the $^4T_1 \rightarrow {}^6A_1$ transition of Mn^{2+} ions and defect-related emissions from ZnS/ZnO.

Using ColorCalculator software, the chromaticity coordinates of the samples were analyzed before and after doping. As shown in Fig. 9c, the undoped ZnS/ZnO sample exhibits coordinates of (0.2013, 0.3765), falling in the cyan region, whereas the ZnS/ZnO: 0.1% Mn^{2+} sample shifts to (0.3490, 0.3693), positioning it in the white light zone. The PL spectral differences across varying Mn^{2+} concentrations ($x = 0$–0.7%) indicate 0.1% as the optimal doping level for warm-white light emission. A performance comparison with previously reported materials,

detailed in Table 4, underscores the suitability of this phosphor for WLED applications.

Fig. 9d illustrates the PL decay curves of ZnS/ZnO:0.1% Mn^{2+} samples at various doping concentrations, excited at 333 nm and monitored at 586 nm. The measured lifetimes, ranging from 0.78 ms to 0.56 ms for 0.3–0.7% Mn^{2+}, reflect the characteristic long-lived emission of Mn^{2+} ions. At lower doping levels, Mn^{2+} ions tend to remain isolated, resulting in longer lifetimes. However, increased concentrations promote Mn–Mn interactions, which enhance non-radiative processes and reduce lifetimes.[47] Interestingly, the 0.1% Mn^{2+} sample exhibits a shorter lifetime of 0.35 ms, likely due to additional emissions from defect states associated with sulfur and oxygen in the host lattice.

Temperature-dependent PL spectra of the ZnS/ZnO:0.1% Mn^{2+} sample (annealed at 1000 °C and excited at 333 nm) are shown in Fig. 10a. As temperature rises from 27 °C to 210 °C, an apparent decrease in emission intensity is observed. As shown in Fig. 10b, the PL intensity retains 24.94% of its initial value at 150 °C, indicating moderate thermal stability. This performance is comparable to that of $NaGa_{11}O_{17}:Mn^{2+}$, which maintains 26.9% under similar conditions[48] and is notably higher
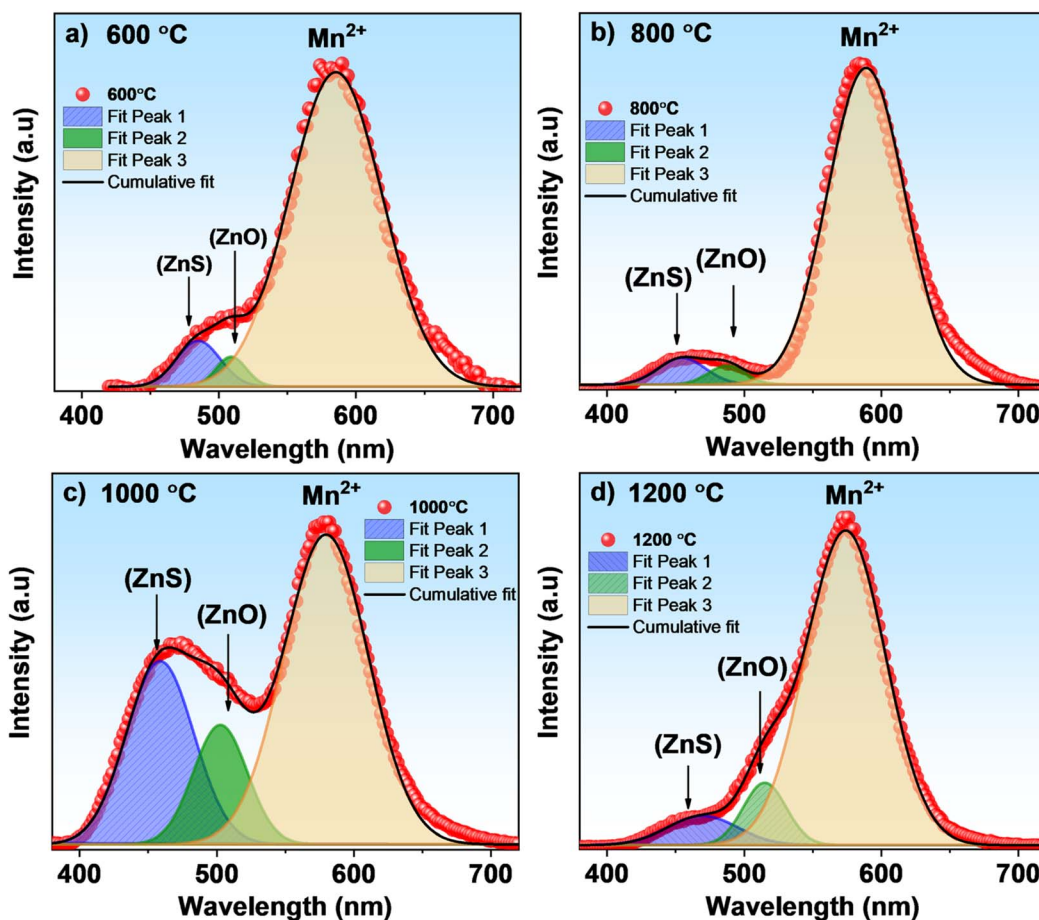
Paper

Fig. 8 Deconvoluted PL spectra of ZnS/ZnO:0.1% Mn^{2+} samples sintered for 2 hours in argon at (a) 600 °C; (b) 800 °C; (c) 1000 °C; and (d) 1200 °C.

Table 3 Emission origin in ZnS/ZnO:Mn^{2+} samples

Intensity (a.u)				
	Temperature (°C)			
Radiation center	600	800	1000	1200
ZnS (vacancy S)	1.65×10^5	3.38×10^6	6.56×10^6	1.53×10^6
ZnO (vacancy O)	6.11×10^4	3.04×10^6	3.89×10^6	1.80×10^6
Mn ($^4T_1 \rightarrow {}^6A_1$)	2.78×10^6	1.73×10^7	1.28×10^7	1.12×10^7

than that of Mn-doped Gd$_3$Ga$_5$O$_{12}$ phosphor, which retains only 21.9%.[49]

The activation energy (ΔE) for thermal quenching was determined using the equation:[50]

$$I = \frac{I_0}{1 + A \, \exp\left(-\dfrac{\Delta E}{k_B T}\right)} \quad (2)$$

where I_0 is the initial PL intensity, I is the intensity at a given temperature, A is a constant, k_B is the Boltzmann constant, and T is the absolute temperature. The inset in Fig. 10b shows a linear fit of $\ln(I_0/I - 1)$ versus $1/T$, from which ΔE was

calculated to be approximately 0.31 eV. This value is higher than that of ZnS/ZnO phosphor (0.26 eV)[15] and aligns well with reported activation energies for other Mn-doped systems, such as MnS/ZnS core–shell (0.393 eV),[51] ZnSe:Mn^{2+} (0.37 eV),[52] ZnS:Mn^{2+} nanocrystalline (0.62 eV).[50]

Fig. 10c shows the electroluminescence (EL) spectra of a 366 nm NUV chip driven at 200 mA, featuring a sharp emission at 366 nm from the chip and a broad visible emission from the ZnS/ZnO:0.1% Mn^{2+} phosphor coating. The 366 nm excitation, slightly red-shifted from the optimal ∼333 nm PLE peak (Fig. 9a), was selected for its commercial availability and ease of integration, despite 333 nm providing stronger photoluminescence but posing challenges in LED availability and stability. The broad emission confirms the phosphor's effective contribution to the visible range. The quantum efficiency (QE), a key performance metric, was calculated using the following equation:[25]

$$QE = \frac{\int I_{em,Vis-LED} - \int I_{em,Vis-Chip}}{\int I_{em,NUV-Chip} - \int I_{em,NUV-LED}} \times 100\% \quad (3)$$

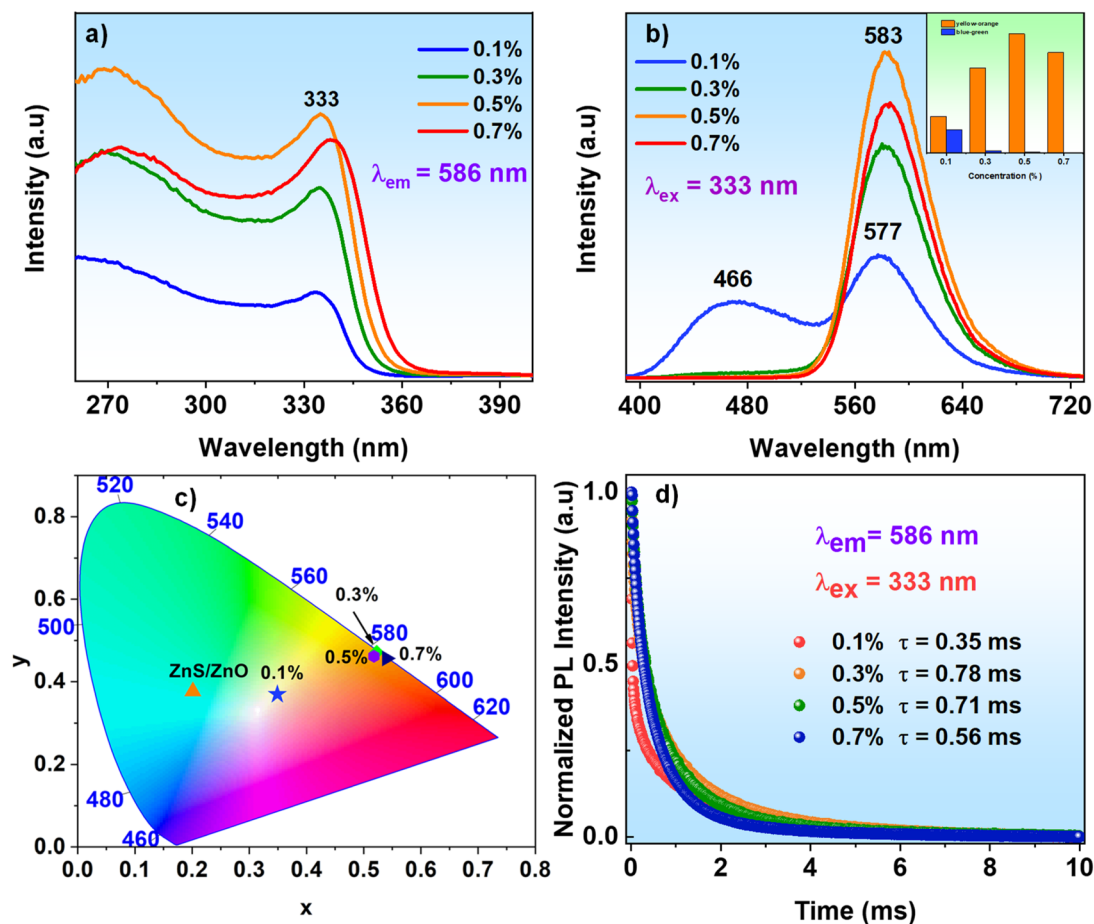Based on this, the ZnS/ZnO:0.1% Mn phosphor annealed at 1000 °C achieved a QE of approximately 29.17%.

Fig. 9   (a) PLE spectra, (b) PL spectra & ratio of emission intensity at peak 466 nm and 586 nm (c) CIE chromaticity coordinate of Zn/ZnO:x Mn^{2+} (x = 0.1–0.7%) and (d) PL decay curves of ZnS/ZnO:x% Mn^{2+} (x = 0.1–0.7) phosphors sintered for 2 hours at 1000 °C in argon.

In addition, the luminous efficacy (lm per W), K, of the LED can be determined using the following formula:[53]

$$K = \frac{\Phi}{P} \qquad (4)$$

where Φ is the luminous flux (41.56 lm), P is the measured electrical power (0.33 W). Based on these values, the luminous efficacy was calculated to be approximately 127.7 lm per W. This is relatively high and comparable to white light emission technologies using micro-LEDs with RGB quantum dots (165 lm per W).[54] It also surpasses the performance reported in several other studies, such as blue LED chips coated with an epoxy:yellow phosphor mixture (97 : 3 wt%), which achieved 23.2 lm per W,[55] or UV LEDs combined with PFO polymer and CdSe/ZnS quantum dots, yielding only 13 lm per W.[56]

The corresponding CIE color coordinates of the fabricated LED are (x, y) = (0.4974, 0.3405), placing it within the warm white region (Fig. 10d), with a correlated color temperature (CCT) of 2506 K. These results highlight the potential of ZnS/ZnO:0.1% Mn^{2+} phosphor as an efficient and promising phosphor for warm-white WLED applications.

Table 4   Emission and excitation peak of various powder manufactured on ZnS, ZnO-based materials

Materials	Fabrication method	Emission peaks (nm)	Excitation peak (nm)	Ref.
ZnS:Mn nanobelts	Thermal evaporation	440, 510, and 577	325	13
ZnS/ZnO:Mn^{2+} nanobelts	Thermal evaporation			13
ZnO:Mn^{2+} nanopowder	Microwave-assisted hydrothermal	620	405	23
ZnS/ZnO micropyramid	Thermal evaporation	500	341	24
ZnS:Mn^{2+} nanoparticles	Co-precipitation	445 and 580	320	45
ZnO:Mn^{2+} nanorods	Thermal evaporation	444 and 575	350	46
ZnS/ZnO: Mn^{2+}composite microphosphors	Thermal diffusion	466 and 586	333	This work

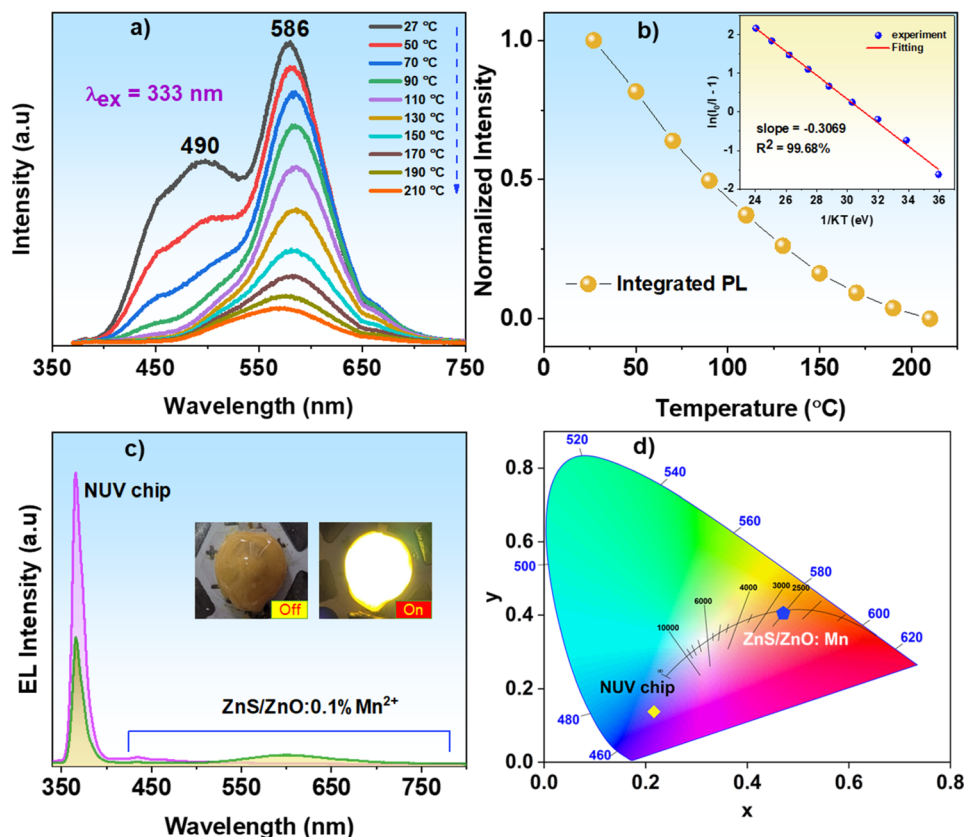© 2025 The Author(s). Published by the Royal Society of Chemistry

Fig. 10 (a) The temperature-dependent PL spectra excited at 333 nm of ZnS/ZnO:0.1% Mn^{2+} phosphors, (b) the corresponding integral normalized PL intensity as a function of temperature. (c) EL spectra of the NUV chip (366 nm) without and with coating a layer of the ZnS/ZnO:0.1% Mn^{2+} phosphor and (d) color coordinates of the fabricated LED.

4 Conclusions

In this work, the full-visible-spectrum ZnS/ZnO:Mn^{2+} phosphors were successfully produced by using a thermal diffusion method. The phosphors exhibit strong absorption in the NUV/UV region, with prominent peaks at 333 nm and 372 nm, and emits a broad emission spanning 400–700 nm. Optimization of Mn^{2+} concentration and annealing temperature identified ZnS/ZnO:0.1% Mn^{2+}, annealed at 1000 °C for 2 hours in argon, as the optimal composition. This sample shows a relatively long decay time of 0.35 ms, moderate thermal stability with 24.94% PL retention at 150 °C, and an activation energy of 0.31 eV. When applied to a 366 nm LED chip, it achieves a quantum efficiency of 29.17%, a CRI of 72, a luminous efficacy of 127.7 lm per W, and warm white emission with CIE coordinates $(x, y) = (0.4974, 0.3405)$ and CTT of 2506 K. These results highlight its strong potential for high-performance warm WLED applications.

Data availability

The data supporting this article have been included as part of the ESI.†

Conflicts of interest

The authors declare no conflicts of interest.

References

1 T. Pulli, T. Dönsberg, T. Poikonen, F. Manoocheri, P. Kärhä and E. Ikonen, *Light:Sci. Appl.*, 2015, **4**, 1–7.

2 M. Bliss, T. R. Betts and R. Gottschalg, *Reliab. Photovoltaics Cells Modules Comps., Syst.*, 2008, **7048**, 704807.

3 K. H. Loo, Y. M. Lai, S. C. Tan and C. K. Tse, *IEEE Trans. Power Electron.*, 2012, **27**, 974–984.

4 L. Chen, C. C. Lin, C. W. Yeh and R. S. Liu, *Materials*, 2010, **3**, 2172–2195.

5 Y. Li, S. Qi, P. Li and Z. Wang, *RSC Adv.*, 2017, 7, 38318–38334.

6 G. Zhou, X. Jiang, M. Molokeev, Z. Lin, J. Zhao, J. Wang and Z. Xia, *Chem. Mater.*, 2019, **31**, 5788–5795.

7 Y. Zhu, C. Li, D. Deng, B. Chen, H. Yu, H. Li, L. Wang, C. Shen, X. Jing and S. Xu, *J. Alloys Compd.*, 2021, **853**, 157262.

8 K. Li, M. Xu, J. Fan, M. Shang, H. Lian and J. Lin, *J. Mater. Chem. C*, 2015, **3**, 11618–11628.

9 K. K. Dubey, V. Nayar and P. S. Choudhary, *Mater. Sci. Res. India*, 2010, **7**, 195–200.

10 X. Fang, Y. Bando, U. K. Gautam, T. Zhai, H. Zeng, X. Xu, M. Liao and D. Golberg, *Crit. Rev. Solid State Mater. Sci.*, 2009, **34**(3–4), 190–223.

11 F. Li, Y. Jiang, L. Hu, L. Liu, Z. Li and X. Huang, *J. Alloys Compd.*, 2009, **474**, 531–535.

12 D. Peipei, L. Dongjie, L. Guogang, A. A. Al Kheraif and L. Jun, *Adv. Opt. Mater.*, 2020, **8**(16), 19011993.

13 D. Q. Trung, M. T. Tran, N. D. Hung, Q. Nguyen Van, N. T. Huyen, N. Tu and H. Pham Thanh, *Opt. Mater.*, 2021, **121**, 111587.

14 R. Mahajan and R. Prakash, *J. Mater. Sci.:Mater. Electron.*, 2022, **33**, 25491–25517.

15 D. Q. Trung, M. T. Tran, N. Van Du, N. D. Hung, T. Thi, H. Tam, N. Tu, P. M. Tri, H. G. Chuc, N. Duc, T. Kien, N. Van Quang and P. T. Huy, *RSC Adv.*, 2025, 616–627.

16 M. T. Tran, D. Quang Trung, N. Tri Tuan, N. T. Tuan, N. Tu, N. Van Du, N. Duy Hung, N. Van Quang, T. Thi Hao Tam, N. D. Trung Kien, N. M. Hieu and P. T. Huy, *Dalton Trans.*, 2023, **52**, 12704–12716.

17 M. Pudukudy and Z. Yaakob, *Appl. Surf. Sci.*, 2014, **292**, 520–530.

18 Y. Cheng, R. Chen, H. Feng, W. Hao, H. Xu, Y. Wang, J. Li, F. Li, S. Zhang and H. Sun, *Phys. Chem. Chem. Phys.*, 2014, **16**, 4544.

19 M. Sundararajan, P. Sakthivel and A. C. Fernandez, *J. Alloys Compd.*, 2018, **768**, 553–562.

20 D. Son, D. R. Jung, J. Kim, T. Moon, C. Kim and B. Park, *Appl. Phys. Lett.*, 2007, **90**, 88–91.

21 B. Zhu, Q. Zhang, X. Li and H. Lan, *Phys. Status Solidi A*, 2018, **215**, 1–6.

22 B. S. R. Devi, R. Raveendran and A. V. Vaidyan, *Pramana - J. Phys.*, 2007, **68**, 679–687.

23 F. C. Romeiro, J. Z. Marinho, A. C. A. Silva, N. F. Cano, N. O. Dantas and R. C. Lima, *J. Phys. Chem. C*, 2013, **117**, 26222–26227.

24 D. Q. Trung, M. T. Tran, N. Tu, L. T. H. Thu, N. T. Huyen, N. D. Hung, D. X. Viet, N. D. T. Kien and P. T. Huy, *Opt. Mater.*, 2022, **125**, 1–11.

25 D. Q. Trung, N. V. Quang, M. T. Tran, N. V. Du, N. Tu, N. D. Hung, D. X. Viet, D. D. Anh and P. T. Huy, *Dalton Trans.*, 2021, **50**, 9037–9050.

26 M. A. Avilés, J. M. Córdoba, M. J. Sayagués and F. J. Gotor, *J. Mater. Sci.*, 2020, **55**, 1603–1613.

27 F. I. H. Rhouma, F. Belkhiria, E. Bouzaiene, M. Daoudi, K. Taibi, J. Dhahri and R. Chtourou, *RSC Adv.*, 2019, **9**, 5205–5217.

28 P. Schröer, P. Krüger and J. Pollmann, *Phys. Rev. B: Condens. Matter Mater. Phys.*, 1993, **47**, 6971–6980.

29 N. X. Sang, N. T. P. Anh, N. D. Dung, N. H. C. Huy, N. H. Tho and L. T. L. Anh, *VNU J. Sci. Math.–Phys.*, 2019, **35**, 69–76.

30 X. Wang, J. Shi, Z. Feng, M. Li and C. Li, *Phys. Chem. Chem. Phys.*, 2011, **13**, 4715–4723.

31 U. P. Gawai, U. P. Deshpande and B. N. Dole, *RSC Adv.*, 2017, **7**, 12382–12390.

32 Ü. Özgür, Y. I. Alivov, C. Liu, A. Teke, M. A. Reshchikov, S. Doğan, V. Avrutin, S. J. Cho and H. Morkọ, *J. Appl. Phys.*, 2005, **98**, 1–103.

33 M. A. Kamran, A. Majid, T. Alharbi, M. W. Iqbal, M. W. Amjad, G. Nabi, S. Zou and B. Zou, *J. Mater. Chem. C*, 2017, **5**, 8749–8757.

34 C. Bi, L. Pan, M. Xu, J. Yin, Z. Guo, L. Qin, H. Zhu and J. Q. Xiao, *Chem. Phys. Lett.*, 2009, **481**, 220–223.

35 X. Liu, X. Chen, X. Cui and R. Yu, *Ceram. Int.*, 2014, **40**, 13847–13854.

36 Y. Tong, F. Cao, J. Yang, P. Tang and M. Xu, *Mater. Lett.*, 2013, **94**, 124–127.

37 J. Cao, J. Yang, Y. Zhang, Y. Wang, L. Yang and D. Wang, *Opt. Mater.*, 2010, **32**, 643–647.

38 E. A. Batista, A. C. A. Silva, T. K. de Lima, E. V. Guimarães, R. S. da Silva and N. O. Dantas, *J. Alloys Compd.*, 2021, **850**, 156611.

39 D. Q. Trung, N. T. Tuan, H. V. Chung, P. H. Duong and P. T. Huy, *J. Lumin.*, 2014, **153**, 321–325.

40 A. Kanti Kole, C. Sekhar Tiwary and P. Kumbhakar, *J. Mater. Chem. C*, 2014, **2**, 4338–4346.

41 N. Tu, D. Q. Trung, N. D. T. Kien, P. T. Huy and D. H. Nguyen, *Phys. E*, 2017, **85**, 174–179.

42 P. C. Patel, S. Ghosh and P. C. Srivastava, *Mater. Res. Bull.*, 2016, **81**, 85–92.

43 S. Adachi, *J. Lumin.*, 2023, **263**, 119993.

44 T. Chanier, F. Virot and R. Hayn, *Phys. Rev. B: Condens. Matter Mater. Phys.*, 2009, **79**(20), 205204.

45 G. Murugadoss, B. Rajamannan and V. Ramasamy, *J. Lumin.*, 2010, **130**, 2032–2039.

46 Y. Tong, F. Cao, J. Yang, P. Tang and M. Xu, *Mater. Lett.*, 2013, **94**, 124–127.

47 T. W. Kang, K. W. Park, G. Deressa and J. S. Kim, *J. Lumin.*, 2018, **194**, 551–556.

48 G. Lu, Y. Wang, K. Ma, X. Chen, W. Geng, T. Liu, S. Xu, J. Zhang and B. Chen, *Ceram. Int.*, 2024, **50**, 16190–16200.

49 K. T. Thu, V. D. Huan, N. Tu, D. Q. Trung, N. Van Du, N. Van Quang, T. N. Bach, L. T. Ha, N. D. Hung, D. X. Viet, N. T. Tuan, N. M. Hieu, M. T. Tran and P. T. Huy, *RSC Adv.*, 2025, **15**, 8275–8286.

50 J. F. Suyver, S. F. Wuister, J. J. Kelly and A. Meijerink, *Nano Lett.*, 2001, **1**, 429–433.

51 D. F. Fang, X. Ding, R. C. Dai, Z. Zhao, Z. P. Wang and Z. M. Zhang, *Chin. Phys. B*, 2014, **23**(12), 127804.

52 X. Yuan, J. Zheng, R. Zeng, P. Jing, W. Ji, J. Zhao, W. Yang and H. Li, *Nanoscale*, 2014, **6**, 300–307.

53 Z. P. Rimbawati, H. Alam and M. Irwanto, *J. Phys.: Conf. Ser.*, 2021, **1811**, 012106.

54 H. V. Han, H. Y. Lin, C. C. Lin, W. C. Chong, J. R. Li, K. J. Chen, P. Yu, T. M. Chen, H. M. Chen, K. M. Lau and H. C. Kuo, *Opt. Express*, 2015, **23**(25), 32504–32515.

55 C. S. Son, H. J. Chang, K. H. Jaekal, Y. C. Chang and S. W. Lee, *Mater. Sci. Forum*, 2006, **510**, 106–109.

56 K. J. Chen, Y. C. Lai, B. C. Lin, C. C. Lin, S. H. Chiu, Z. Y. Tu, M. H. Shih, P. Yu, P. T. Lee, X. Li, H. F. Meng, G. C. Chi, T. M. Chen and H. C. Kuo, *Opt. Express*, 2015, **23**(7), A204–A210.